Input Parameters for the Simulation of Silicon Solar Cells in 2014

Andreas Fell, Keith R. McIntosh, Pietro P. Altermatt, Gaby J. M. Janssen, Rolf Stangl, Anita Ho-Baillie, Heiko Steinkemper, Johannes Greulich, Matthias Müller, Byungsul Min, Kean C. Fong, Martin Hermle, Ingrid G. Romijn, and Malcolm D. Abbott

(Review Paper)

***Abstract*—Within the silicon photovoltaics (PV) community, there are many approaches, tools, and input parameters for simulating solar cells, making it difficult for newcomers to establish a complete and representative starting point and imposing high requirements on experts to tediously state all assumptions and inputs for replication. In this review, we address these problems by providing complete and representative input parameter sets to simulate six major types of crystalline silicon solar cells. Where possible, the inputs are justified and up-to-date for the respective cell types, and they produce representative measurable cell characteristics. Details of the modeling approaches that can replicate the simulations are presented as well. The input parameters listed here provide a sensible and consistent reference point for researchers on which to base their refinements and extensions.**

***Index Terms*—Photovoltaic (PV) cells, semiconductor device modeling, silicon solar cells, solar cell simulation.**

I. INTRODUCTION

DEVICE simulation helps photovoltaics (PV) researchers to understand solar cells, to perform loss analyses, to predict how changes to a solar cell design or fabrication procedure will affect its efficiency, and to provide a quantitative foundation to decide on R&D strategies. In their timeless quest to increase accuracy (and reduce complexity), researchers have generated a plethora of equations, algorithms, parameterizations, and programs to simulate solar cells. To the newcomer, the vast array of approaches and possible inputs can be confounding. To the old timer, it is tedious to state all of the inputs and assumptions that ensure a fellow researcher can replicate and test their simulations.

We seek to alleviate these problems by providing a set of inputs to simulate six major types of silicon solar cells. The input sets comprise a starting point for new comers and provide a reference point from which researchers can base their refinements and extensions. The input sets contain the physical properties of the cells, and as such, they are not specific to any modeling approach or software tool.

In addition to providing parameter sets, we apply a specific modeling approach and set of software tools to simulate the optical and electrical behavior of the solar cells. It presents a balance between a high level of detail to cover detrimental physical effects and a low level of complexity to be reproducible and comprehensible to nonexperts. Notably, a subset of the used software tools is freely available, providing a readily accessible way to reproduce the presented results.

The first two parameter sets represent industrial screen-printed solar cells. Due to issues of commercial confidentiality, compromises are made in the selection of values to make public here. Most notably, the inputs that define the emitter profiles and metallization are more representative of recent forerunners to modern industrial cells, rather than those produced in 2014. Nevertheless, the datasets provide a complete and sensible starting point from which readers can critically examine, debate, and substitute inputs. No such compromises are made in the remaining four parameter sets, which represent laboratory-based solar cells whose structures and behavior have been published in detail. A preliminary version of the first parameter set was published in [1].

For completeness, the text that follows is replete with assumptions and qualifiers, many of which require a background in solar cell physics to comprehend. The new comer need not be discouraged by this level of detail. They can commence by downloading the parameter sets from an online solar cell library [2], varying the inputs in the appropriate software and
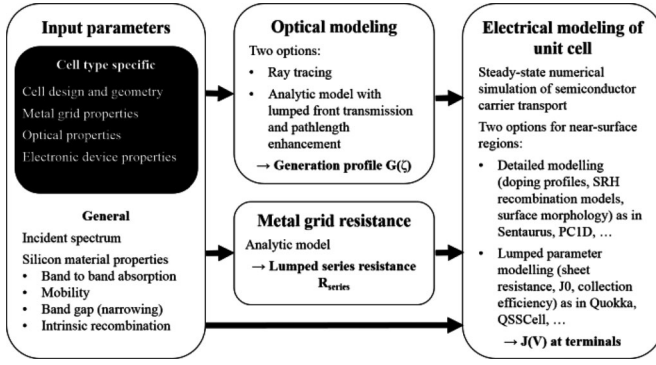
Fig. 1. Flowchart describing the modeling approach; highlighted are the cell-type specific input parameters which form the scope of this work.

observing how the efficiency of a particular cell type depends on its physical structure.

II. MODELING APPROACH

The modeling approach followed in this work is sketched in Fig. 1. It can be divided into optical modeling to derive the generation profile, calculation of a lumped series resistance to represent the metal grid resistive losses, and electrical simulation of an element of symmetry (a unit cell). For the sake of keeping complexity at a moderate level, this approach neglects some full-size effects: perimeter losses, busbar recombination, the distributed nature of the metal grid resistance, and inhomogeneity of the silicon wafer. Details of the assumptions and simplifications are stated in the following sections.

A. Optical Modeling

The purpose of the optical modeling is to determine the generation profile of electron–hole pairs within the silicon. This requires knowledge of the incident illumination, the surface morphologies, the thickness of the wafer and any films, and the complex refractive index of all materials.

Parameter sets for two modeling approaches are presented. Importantly, both approaches modify the generation profile under textured surfaces such that it approximates the profile under an equivalent planar surface. It greatly simplifies the subsequent electrical modeling to treat the solar cell as having planar surfaces.

The first approach is ray tracing, here performed with *Sentaurus Device* [3] or the Wafer ray tracer on PV Lighthouse [4]. Both are able to directly compute the generation profile $G(\zeta)$ of electron–hole pairs in the silicon, where ζ is defined as the shortest distance to the illuminated surface [5]. The purpose of using ζ rather than depth is that it converts the generation profile under a complicated geometry (e.g., random pyramids) to an equivalent generation profile under a planar surface.

The second approach to the optical modeling is to use the front-surface transmission $T_{\text{ext}}(\lambda)$ and the pathlength enhancement $Z(\lambda)$ as inputs, which are both a function of wavelength λ. As described in detail in [6], those quantities are used to calculate the generation profile by an analytical model similar to the one presented in [7] and are suitable inputs, e.g., for the solar cell simulator Quokka [8]. Furthermore, the related reflection,

absorption, and transmission data are used for comparison to quantum efficiency (QE) measurements of finished solar cells, with the purpose of validating and calibrating the optical and electrical input parameters.

Shading by fingers is represented by nil generation underneath their effective shading width, whereas busbar shading is considered by either a global scaling of the generation profile or a postsimulation scaling of the current density, which gives almost identical results. The influence of altered internal reflectivity at finger and busbar regions is neglected for simplicity. Furthermore, free-carrier absorption and photon reabsorption are neglected or effectively incorporated into rear reflector assumptions to fit measured J_{sc}.

B. Metal Grid Resistance

The metal grid resistance is represented by a lumped series resistance value R_{series}, thereby neglecting the influence of its distributed nature. This can overestimate the fill factor (FF) for cells that have a significant metal resistance, but for the cells presented here, it was concluded from SPICE modeling that the assumption has minimal influence on FF. R_{series} is derived by analytical modeling, as described in [9], using Grid on PV Lighthouse. Contact resistance is excluded from the lumped series resistance because it is included in the electrical modeling, thereby accounting for related current transfer effects. Busbar resistance is neglected, which is consistent with a high number of measurement probes along the busbar during current–voltage testing. Unless stated otherwise, a rectangular profile of metal fingers is assumed.

C. Electrical Modeling of the Unit Cell

To derive the current–voltage (*I*–*V*) and QE characteristics of the solar cell, electrical modeling of the unit cell is performed by means of steady-state numerical simulation of the semiconductor carrier transport in two or three dimensions. There are essentially two different ways of treating near-surface regions: 1) lumped parameter modeling (i.e., the conductive boundary approach) and 2) detailed modeling.

The first approach has the advantage of being simpler and much faster. The near-surface region is treated as a boundary condition, described by a set of lumped input parameters consisting of the sheet resistance R_{sheet}, the collection efficiency η_{c}, and a (injection-dependent) recombination parameter J_0 or S_{eff}. It is well validated for typical wafer-based silicon solar cells and implemented in several software tools, e.g., in Quokka [8], [10], CoBoGUI [11], PC2D [12], and QSSCell [13], [14].

The second approach is more computationally expensive, but it includes the physical nature of the surfaces and immediate subsurface regions. It simulates them by solving a set of best-known physical models that describe the electrical, optical, and thermal properties of the material system. The main inputs for solar devices are the doping profile $N(\zeta)$, the surface Shockley–Read–Hall (SRH) recombination parameters S_{n} and S_{p}, the surface charge Q, and at times empirical correction factors in case of a textured surface morphology. This approach provides more insight into the detailed operation of the device and must be used when effects within the near-surface regions are investigated. It

is well established and implemented in several software tools, e.g., in Sentaurus Device [3], Atlas [15], EDNA [16], in the Semiconductor Module of Comsol Multiphysics [17], [18] and PC1D [19], [20].

As described in Section II-A, a textured surface is approximated by a planar electrical solution domain, which for the detailed modeling necessitates the introduction of correction factors to reproduce experimentally measured characteristics. Most importantly, the recombination increases due to surface area enlargement, which is addressed by increasing recombination parameters, mainly S_{n0} and S_{p0}, and optionally volumetric Auger and SRH recombination by a texture multiplier (typically 1.3–1.7). While the measured J_0 can be reproduced by this approach, an accurate representation of the collection efficiency η_c (ratio of collected and generated carriers within the near-surface region) is difficult to achieve simultaneously. The conductive boundary approach avoids this problem by setting J_0, R_{sheet}, and η_c independently of one another to empirically determined values. Due to zero generation underneath fingers, η_c for contacted regions is irrelevant and consequently not given in the input parameter sets.

It is also possible to use a combined approach in which aspects of the cell that cannot be directly measured are first simulated with detailed modeling, and then, the lumped outputs are used in a subsequent conductive boundary model.

In this paper, we describe how each solar cell structure can be consistently simulated with both the lumped parameter and detailed approach. For lumped parameter modeling, we use a combination of EDNA [16] to perform detailed surface modeling (where lumped parameters are not directly available) and *Quokka* [8] for conductive boundary device simulations. Complete detailed modeling is performed with the commercial device simulation software Sentaurus Device [3] or Atlas [15].

In this work, the simulation of the electrical performance of the unit cell neglects some of the specific regions of a real solar cell. Most notable is the impact of the busbar and edge regions. In addition, some solar cells also have solder contact pads that can introduce additional recombination due to the lack of BSF formed. In all of the front-contact simulations presented here (except the PERL cell which has no busbar), the impact of the busbar shading is considered as described in the Section II-A. For simplicity, the recombination impact of these regions is neglected as is any impact from the edge regions. Furthermore, any J_{02} and R_{shunt} contributions from edges and busbars are neglected, again for simplicity.

III. INPUT PARAMETER SETS

The main purpose of this work is to present complete and representative parameter sets for six major silicon solar cell structures. The first two sets are for common commercial solar cells, and the other four sets are laboratory-based solar cells. The input parameters comprise a mixture of measured, modeled, and empirically fitted values, as stated for the individual cell types.

We emphasize that the input parameters cannot provide a precise description of every solar cell of a given structure. The PV industry manufactures cells with a wide distribution of *I–V* performance, largely due to a wide distribution in the quality

TABLE I
GENERAL INPUT PARAMETERS USED IN THIS WORK

Temperature	298.15 K (25 °C)
free carrier statistics	Fermi–Dirac for highly doped regions Boltzmann for bulk (equals Fermi–Dirac for low doping)
intrinsic carrier density	8.27×10^9 cm^{-3} (calculated from [eq. (3), 23] multiplied by 0.9953 to match 9.65×10^9 cm^{-3} at 300 K [24])
bandgap narrowing	no BGN for bulk in conductive boundary modeling, Schenk [25] otherwise
Auger recombination	Richter *et al.* [26] (300 K)
radiative recombination	$B_{\text{rad}} = 4.73 \times 10^{-15}$ cm^3/s [27] (300 K)
mobility	Klaassen [28]
incident spectrum	AM1.5g [29]
optical properties Si	Green [30]

of silicon wafers but due to ongoing improvements in materials, equipment and processes and to temporal variability in production lines as well.

The parameter sets provided for the industry-typical cells (A, B) are necessarily nebulous. They are not generated from any specific solar cell, but are selected to represent a "typical" cell within the wide variety manufactured in industry. The parameter sets do not represent the "state-of-the-art" in 2014, and they will be outdated in the near future. In fact, some inputs could already be considered outdated, a necessary consequence of commercial confidentiality. To supplement the specific values, we therefore provide a value range for those inputs that are well known to have a wide distribution.

The parameter sets for the laboratory-based cells (C–F) are more specific because, with the exception of the heterojunction technology (HJT) cell (D), they have been determined from measurements on a particular experimental solar cell. The inputs for the HJT cell combine properties from different laboratories (not industry). Thus, the laboratory-based cells are very specific to the technology applied by the respective institute and are also not representative of their equivalent industrial solar cells.

Thus, irrespective of the dataset, the reader is encouraged to use these inputs as a sensible and consistent starting point and to substitute their own values where appropriate.

General Input Parameters

An essential part of the input parameters form the general inputs common to all cell types, including the choice of parameterizations for modeling silicon properties. Table I summarizes the inputs used in this work, mostly as suggested in [21]. Notably, for Auger and radiative recombination, model parameters are valid at 300 K only. However, neglecting their temperature dependence results in minor effect on the simulation result compared with the large effect of the different intrinsic carrier concentration. We accept these inconsistencies and choose 25 °C (298.15 K) to be more representative for standard testing conditions.

An important parameter for the conductive boundary modeling using J_0 values is the effective intrinsic carrier density n_{ieff}. We use the value of $n_{\text{ieff}} = n_i = 8.27 \times 10^9$ cm^{-3} (see Table I) in the bulk consistently throughout this work for conductive boundary modeling, neglecting the small amount of bandgap

TABLE II
INPUT PARAMETER SET FOR THE CONVENTIONAL CELL

cell design	
cell size	156 mm × 156 mm square thickness 180-μm
front	homogeneous n$^+$ diffusion H-pattern screen-printed metallization
rear	full-area screen-printed and alloyed Al-BSF
optics	
front dielectric	80-nm PECVD SiN$_x$ [43] ($n = 1.99$)
front morphology	Isotexture, modeled by spherical caps with $\omega = 60°$ [33]–[35]
busbar shading fraction	2.5%
effective finger shading width	42 μm (finger width times 70% optical shading factor [44])
rear	planar with some scattering, modeled by Phong reflection with $R_0 = 0.7$ and $w = 4$ [45], [46]
metal grid	
front fingers	75 fingers with 2.08-mm-pitch, 60-μm-wide, and 12-μm-high rectangular shape
	Ag-paste with 4.5-$\mu\Omega \cdot$ cm resistivity
	contact resistivity 2-m$\Omega \cdot$ cm^2
	lumped series resistance: 0.312 $\Omega \cdot$ cm^2
front busbars	3 busbars, 1300-μm-wide and 15-μm-high
	Ag-paste with 4.5-$\mu\Omega \cdot$ cm resistivity
	lumped series resistance: neglected
rear metal	full area Al-paste with 35-$\mu\Omega \cdot$ cm resistivity, 30-μm-high
	contact resistivity 5-m$\Omega \cdot$ cm^2
	lumped series resistance: neglected
electrical properties	
bulk	2-$\Omega \cdot$ cm p-type mc mid-gap SRH lifetimes $\tau_n = \tau_p = 75\ \mu$s
front n$^+$ diffusion	*lumped inputs*
	sheet resistance 75 Ω (70–90)
	recombination parameter J_0
	passivated: 201 fA/cm^2 (150–300)
	contacted: 204 fA/cm^2 (200–600)
	depth 0.39 μm
	collection efficiency 0.85 (0.8–0.9).
	detailed inputs
	doping profile
	total and active concentration from [38], see Appendix B
	surface SRH
	passivated: $S_p = 6.63 \times 10^6$ cm/s, $S_n = 1 \times 10^7$ cm/s (derived from [39] with texture multiplier of 1.73)
	contacted: $S_p = S_n = 1 \times 10^7$ cm/s (thermal velocity)
	volume SRH
	modeled via inactive phosphorus profile according to [39] and a texture multiplier of 1.73
rear p$^+$ region	*lumped inputs*
	sheet resistance 30 Ω (20–40)
	recombination parameter $J_0 = 517$ fA/cm^2 (300–700)
	depth 7-μm
	collection efficiency 0.7
	detailed inputs
	doping profile
	measured active concentration from [40] with incomplete ionization model from [45], see Appendix B
	surface SRH
	$S_p = S_n = 1 \times 10^7$ cm/s (thermal velocity)
	volume SRH
	modeled as in [41] with parameters in [42]

narrowing. J_0 values derived with a different assumption of n_{ieff} are scaled according to $J_0/n_{\text{ieff}}{}^2 = \text{const}$ [22].

A. *Conventional (Industry Typical Properties): p-Type Full-Area Rear-Alloyed Cell with Screen-Printed Metallization*

Solar cells with a conventional design are presently the dominant cell type in large-scale industrial manufacturing [31]. The models presented here are based on values obtained from both the literature, as well as various industry sourced cells whose specific details remain hidden for commercial reasons. In general, there are several possible varieties of this cell type. Most notably, the substrate may be either multicrystalline (standard or high performance) or monocrystalline Czochralski (Cz). Here, we have chosen standard multicrystalline material to demonstrate both a simple bulk model for this material as well as how to incorporate an isotextured front surface. The emitter may be formed with either a "standard" or "high-efficiency" approach; see, for example, [32]. We have chosen the "standard" approach to demonstrate how to model the impact of Si–P precipitation on cell performance. It should be noted that, particularly for conventional screen print cells on monocrystalline material, it is likely that the majority of production cells now use the high-efficiency emitter approach. For the input parameters to such an emitter, see the passivated emitter rear cell (PERC) cell in the next section. Finally, the screen-print fingers themselves also have several varieties. This includes single print and double print, as well as an alternative in stencil printing. Since the overwhelming majority of production cells are currently manufactured by the first option, the inputs we present for the front contact represent a typical single-print 3 busbar H pattern with an average finger width that is consistent with the 2014 ITRPV [31].

The front-surface optical properties of these cells are dominated by the isotexture. Although this surface topology is rather irregular and depends strongly on the manufacturing process, it is possible to quantify the photogeneration and parasitic absorption of the cell with standard ray tracing, assuming a 3-D symmetry element with a top shape of a spherical cap spanning a characteristic angle [33]–[35]. The rear interface is approximated with a planar geometry, causing a moderate amount of scattering described with Phong's model [36].

The isotexturing also increases the surface area and, hence, the J_0 of the emitter, typically by a factor of about 1.2. In this simulation example, J_0 derived by detailed modeling in the planar simulation domain without correction factors consequently needs to be 167 fA/cm^2 to represent the target value of 200 fA/cm^2. This increase in J_0 cannot be reproduced by simply increasing the SRH recombination velocity S_p of the front surface and the capture cross section σ_p of the inactive phosphorus by a factor of 1.2, because the limited carrier collection efficiency causes nonlinearities. In our example, a suitable multiplication factor turned out to be 1.73 (coincidentally the surface area enhancement factor of ideal pyramidal texture). This quantifies V_{oc} rather precisely, but then underestimates the internal quantum efficiency in the UV and blue part of the spectrum. For the conductive boundary modeling, we therefore do not use the collection efficiency resulting from the detailed modeling of this particular emitter but, rather, a typical constant value of 0.85 [32], [37].

The "standard" heavily doped emitter is modeled using both a profile of active as well as inactive dopants as shown in Fig. 6 in Appendix B. The difference between these two profiles is inactive phosphorus (interstitial P clusters and possibly various forms of precipitates), which then leads to a highly localized degradation of the carrier lifetime. The full details of these profiles and their impact on recombination can be found in [38]

and [39]. Notably, we neglect the effects of metal paste etching and silver crystallites under at the contacted emitter regions, but rather assume identical doping profiles with thermal surface recombination velocity. This may result in an unrealistically low J_0 for the contacted emitter, which has however minor influence on the simulated cell characteristics.

Similarly, we present a detailed model for the back surface field. This work has assumed that the boron concentration of the screen-printed pastes is negligible (which may not be true for high-efficiency rear-side pastes), and therefore, the BSF is entirely formed from Al. The exact profile used for the BSF is obtained from [40] and is shown in Fig. 7 in Appendix B. The modeling accounts for incomplete ionization and Al–O complex recombination via the models presented in [41], with defect parameters taken from [42].

The lifetime within the bulk of multicrystalline material is dominated by a variety of defects, which are expected to vary greatly from wafer to wafer. For this reason, we propose here a simplification which will allow the simulation of the basic underlying performance of the device architecture itself. Neglected are the spatial variations of the bulk lifetime due to the different grains, grain boundaries, edge contaminated regions, and defect clusters. It is worth noting that the relative impact of all of the inputs will be modulated by this underlying material quality. However, specific strategies to account for this are beyond the scope of this paper. Thus, to provide a basic model for the bulk of a standard mc-Si wafer, we use here a single SRH defect at mid-band with $\tau_n = \tau_p = 75\ \mu s$. The input parameters for the conventional cell are summarized in Table II.

B. Passivated Emitter Rear Cell (Industry Typical Properties): Monocrystalline p-Type Cell With Local Al-BSF and Screen-Printed Metallization

PERC cells are presently being introduced into mass production to increase cell efficiency. They improve upon the conventional cell (described above) by replacing the rear-surface full-area Al-BSF with a stack of passivation layers and localized contacts; in order to gain benefits from the improved rear, the emitter must be improved as well. The localized contact regions are typically formed by locally laser ablating the rear dielectric film and then firing specialized screen-printed Al paste through the openings to form localized BSF regions.

In principle, the rear of the PERC cell architecture is somewhat independent of the choice of front-surface properties. As such, it would be possible to substitute the values provided here with those from the previous section. However, the low recombination achieved at the rear surface means that this type of cell is more sensitive to increased recombination in the bulk or at the front surface. We, therefore, model it with a "high-efficiency" emitter and good-quality monocrystalline Cz silicon substrates. The SRH lifetime parameters are chosen from [47] and do not include the recent improvements made in stabilizing the B–O complex.

The optical losses are calculated with standard ray tracing assuming a classic single KOH textured pyramid but random shifts of the rays to mimic the random placement of the pyra-mids. The optical properties of the rear interface are important in PERC cells. In this example, the scattering and parasitic absorption are ray traced with the tilted-mirrors model [48], [49]. The optical properties depend strongly on the thickness of the dielectric between Si and Al. Here, a 100-nm SiN_x is chosen (having the same refractive index as the front AR coating for simplicity), on top of 10-nm plasma-enhanced chemical vapor deposition (PECVD) AlO_x.

For confidentiality reasons, the "high-efficiency" emitter used here does not represent an actual manufactured one. It is derived from the "standard" emitter as described in the above conventional cell by omitting the first 30 nm of the doping profile, representing an etch-back process commonly used in industry for this purpose, and as such might be significantly different to typical high-efficiency emitter profiles. The KOH-texturing increases the surface area of the emitter by a factor of approximately 1.7. It is shown in [50], however, that the accompanying increase in J_0 can be reasonably compared with the increase in case of isotexturing. Therefore, for calculating the SRH recombination velocity S_p of the front side and the capture cross section σ_p of the inactive phosphorus, we choose a texture multiplier of 1.35, which is used to account for the increase in J_0 of many industrial emitters after isotexturing. Detailed modeling of this virtual "high-efficiency" emitter results in a typical decrease of J_0 compared with the standard emitter (while still having a slightly higher than typical absolute value) but with a notably relatively high sheet resistance R_{sheet}. Due to the latter, the simulated resistive losses in the emitter may be larger than typical. As explained in the conventional cell above, the collection efficiency is set independent from the detailed modeling results to a value of 0.95 typical for a high-efficiency emitter.

Of critical importance to the performance of a PERC cell is the design of the rear-side contact pattern. The localized BSF regions are in this case formed as lines but are often also formed as an array of points. The selection of the width and pitch of these lines is a tradeoff between resistive and recombination losses. From the literature, it is clear that there is a wide variety of values for the recombination at the rear surface and within these localized contact regions. However, insufficient reliable data have been published to date to deduce a justifiable range for J_0 of the localized BSF, which is therefore omitted from Table III despite its large variation. The amount of recombination within the device may also be affected by void formation, which is not accounted for here. In this example, we neglect lateral variations within the localized BSF regions and apply the full-area Al-BSF profile from the conventional cell above thinned by 3 μm to represent the typically shallower depth and higher recombination of a localized BSF. The input parameters for the PERC cell are summarized in Table III.

C. n-PASHA (ECN): Bifacial n-Type Cell with Screen- and Stencil-Printed Metallization

The n-PASHA cell developed at ECN [53], along with its industrial equivalents PANDA of Yingli Solar [54], is one of the most prominent industrial bifacial cells. The models and input sets presented here for the n-Pasha cell have been chosen

cell design	
cell size	156 mm × 156 mm pseudosquare thickness 180 μm
front	homogeneous n^+ diffusion H-pattern screen-printed metallization
rear	undiffused and passivated line local p^+ alloyed Al-BSF, 120 μm wide, 850 μm pitch
optics	
front dielectric	70-nm PECVD SiN_x [43] ($n = 1.99$)
front morphology	random pyramids
rear dielectrics	10-nm PECVD Al_2O_3 [51] (inner film) 100-nm PECVD SiN_x [43] ($n = 1.99$) (outer film)
rear morphology	modeled by "strong planarization" case of the tilted-mirrors model [48], [49]
busbar shading fraction	2.5%
effective finger shading width	42 μm (finger width times 70% optical shading factor [44])
metal grid	
front fingers	91 fingers with 1.7 mm pitch, 60 μm wide, and 12 μm high, rectangular shape Ag-paste with 4.5-$\mu\Omega \cdot$cm resistivity contact resistivity 2 m$\Omega \cdot$cm^2 lumped series resistance: 0.252 $\Omega \cdot$cm^2
front busbars	3 busbars, 1300-μm-wide and 15-μm-high Ag-paste with 4.5-$\mu\Omega \cdot$cm resistivity lumped series resistance: neglected
rear metal	full area Al-paste with 35-$\mu\Omega \cdot$cm resistivity, 30-μm-high contact resistivity 5-m$\Omega \cdot$cm^2 lumped series resistance: neglected
electrical properties	
bulk	2-$\Omega \cdot$cm p-type CZ mid-gap SRH lifetimes $\tau_n = 371$ μs and $\tau_p = 3710$ μs derived from [47]

front n^+ diffusion	*lumped inputs*
	   sheet resistance 162 Ω (90–160)*
	   recombination parameter J_0
	     passivated: 168 fA/cm^2 (80–140)*
	     contacted: 595 fA/cm^2 (400–700)
	   depth 0.36 μm
	   collection efficiency 0.95
	 detailed inputs
	   doping profile
	     total and active concentration from [38] with 30-nm etch-back, see Appendix B
	   surface SRH
	     passivated: $S_p = 4.86 \times 10^5$ cm/s, $S_n = 1 \times 10^7$ cm/s (derived from [39] with texture multiplier of 1.35)
	     contacted: $S_p = S_n = 1 \times 10^7$ cm/s (thermal velocity)
	   volume SRH
	     modeled via inactive phosphorus profile according to [39] and a texture multiplier of 1.35

rear p^+ region	*lumped inputs*
	   sheet resistance 61-Ω
	   recombination parameter $J_0 = 795$ fA/cm^2
	   depth 4 μm
	   collection efficiency 0.9
	 detailed inputs
	   doping profile
	     measured active concentration from [40] with incomplete ionization model from [45], 3-μm etch-back; see Appendix B
	   surface SRH
	     $S_p = S_n = 1 \times 10^7$ cm/s (thermal velocity)
	   volume SRH
	     modeled as in [41] with parameters in [42]

TABLE III
(CONTINUED)

passivated rear	*lumped inputs*
	   recombination parameter $J_0 = 13.1$ fA/cm^2
	 detailed inputs
	   surface SRH and charge
	     $S_p = 78$ cm/s, $S_n = 1.08 \times 10^5$ cm/s, $Q = -3 \times 10^{12}$ cm^{-2} from [52] with $D_{it} = 6 \times 10^{17}$ cm$^{-2} \cdot$eV^{-1} (midgap)

*The lumped input parameters for the emitter being out-of-range of typical values is caused by the enforced consistency with the detailed modeling, which input parameters deviate from an industry-typical high-efficiency emitter due to confidentiality reasons (see text for more information)

such that the optical, recombination, and resistive properties of laboratory cells manufactured at ECN are well represented. A slightly different description of the n-Pasha cell was given in [55].

The reported J_0 values were taken from lifetime measurements. The reported S_{p0}, S_{n0} values were adapted to obtain the measured J_0. To account for the textured surface, an enhancement factor of 1.7 was used both for the Auger and surface recombination. The present parameters still suggest that optimization of the surface is possible.

It was found that in order to describe recombination at the contacts, a local etch-back of the profile must be assumed [49]. Such a uniform effective etch-back is an idealization of the actual damage that is caused by fire-through metallization, especially under the Ag–Al contacts on the emitter. The effective etch depths are chosen to match the difference in implied V_{oc} of the cell before metallization and the measured V_{oc} after metallization.

The n-Pasha cell has a random pyramid texture at the front and rear surfaces. A textured rear is required to obtain a high bifaciality factor. In the present model, the rear dielectric layer is not treated explicitly. A Lambertian rear reflector was assumed, and the reflectivity was adapted to match the measured J_{sc}. In the assumption for the rear reflector, two opposing effects are lumped: the significant free-carrier absorption within the two full-area diffusions, and the current gain from the reflective chuck used in the measurement.

Fig. 4 shows that the recombination at MPP is rather evenly distributed over the bulk, emitter and BSF, although recombination at the metallized areas is relatively large. Further optimization of contacts and diffused regions would make the cell efficiency more dependent on the bulk quality. The rear n+ diffusion of the n-Pasha cell has a large contribution to the resistive losses, which is accepted in order to keep the shaded area small for high bifaciality. The input parameters for the n-PASHA cell are summarized in Table IV.

D. Heterojunction Technology (Projected): n-Type Heterojunction Cell with Screen-Printed Metallization

The HJT was successfully first industrialized by Sanyo, now Panasonic, and holds the current efficiency record for a

TABLE IV
INPUT PARAMETER SET FOR THE n-PASHA CELL

cell design	
cell size	156 mm × 156 mm pseudosquare
	thickness 180-μm
Front	homogeneous p+ diffusion
	H-pattern stencil-printed metallization
Rear	homogeneous n+ diffusion
	H-pattern screen-printed metallization

optics	
front and rear dielectric	70-nm PECVD SiN$_x$ [43] ($n = 1.99$)
front and rear morphology	random pyramids, 54.3° characteristic angle, 5-μm texture height
rear optics	modeled by Lambertian rear reflector with effective $R = 0.78$ and $T = 0.22$ to match J_{sc} measured with a reflective chuck.
busbar shading fraction	2.86%
effective finger shading width	31.5 μm (finger width times 70% optical shading factor [44])

metal grid	
front fingers	72 fingers with 2.05-mm-pitch, 45-μm-wide, and 30-μm-high
	Al-Ag-paste with 4.7-$\mu\Omega \cdot$ cm resistivity
	contact resistivity 3-m$\Omega \cdot$ cm^2 (estimate)
	lumped series resistance: 0.185 Ωcm^2
front and rear busbars	3 busbars, 1500-μm-wide and 10-μm-high
	Ag-paste with 3-$\mu\Omega \cdot$ cm resistivity, noncontacting
	lumped series resistance: neglected
rear fingers	144 fingers with 1.025-mm-pitch, 100-μm–wide, and 10-μm-high
	Ag-paste with 3-$\mu\Omega \cdot$ cm resistivity
	contact resistivity 3-m$\Omega \cdot$ cm^2 (estimate)
	lumped series resistance: 0.083 $\Omega \cdot$ cm^2

electrical properties	
bulk	2.7 $\Omega \cdot$ cm n-type
	mid-gap SRH lifetimes $\tau_n = \tau_p = 1000\ \mu$s
front p+ diffusion	*lumped inputs*
	sheet resistance 68-Ω
	recombination parameter J_0
	passivated: 63 fA/cm^2
	contacted: 1836 fA/cm^2
	depth 0.55 μm
	collection efficiency = 1
	detailed inputs
	active doping profile
	superposition of two Gaussians: 6.19×10^{19} cm^{-3}/ 5.77×10^{19} cm^{-3} peak, 0.045 μm/0.117 μm peak depth, 0.048 μm/0.135 μm depth factor (PC1D definition)
	200-nm etch assumed under contacts
	surface SRH
	texture multiplier of 1.7
	passivated: $S_p = 2 \times 10^3$ cm/s, $S_n = 2 \times 10^3$ cm/s
	contacted: $S_p = S_n = 1 \times 10^7$ cm/s (thermal velocity)
	volume recombination
	SRH same as bulk
	texture multiplier of 1.7 for Auger
rear n+ diffusion	*lumped inputs*
	sheet resistance 171 Ω
	recombination parameter J_0
	passivated: 103 fA/cm^2
	contacted: 1101 fA/cm^2
	depth 0.4 μm
	collection efficiency = 1
	detailed inputs
	active doping profile
	superposition of two Gaussians: 8.75×10^{19} cm^{-3}/ 2.0×10^{19} cm^{-3} peak, 0 μm/0 μm peak depth, 0.018 μm/0.130 μm depth factor (PC1D definition)

TABLE IV
(CONTINUED)

20-nm etch assumed under contacts	
surface SRH	
texture multiplier of 1.7	
passivated: $S_p = S_n = 6 \times 10^4$ cm/s	
contacted: $S_p = S_n = 1 \times 10^7$ cm/s (thermal velocity)	
volume recombination	
SRH same as bulk texture	
multiplier of 1.7 for Auger	

nonconcentrated single-junction silicon solar cell of 25.6% using an IBC design [56]. With a conventional bifacial design, the corresponding heterojunction cell efficiency record (again achieved by Panasonic) is 24.7% [57]. As a comprehensive characterization and description of their device properties is publicly not available, the stated input parameter set describes a theoretical cell, which essentially combines cell design and electrical properties of thin-film a-Si:H layers and interfaces as optimized, measured, and simulated at SERIS [58], [59], with the optical a-Si:H properties and the TCO properties as published by EPFL [60], [61]. For best consistency, we also employ a value for contact resistivity between Ag-paste fingers on this particular TCO, as published in [62].

While not representing a physical manifestation of a real cell, all individual properties and cell characteristics are within reasonable limits of what is typically achieved at research institutes, highlighting common characteristics and loss mechanisms of HJT cells. A notable deviation of the presented laboratory cell design from an industrial HJT design is the full-area silver-based rear metallization, which in industry is commonly replaced by an H-pattern screen printed metallization for bifaciality and cost reasons.

The corresponding simulation input parameters are calibrated twofold: first using published input parameters for heterojunction solar cells by Rahmouni [63] reproducing published results from Panasonic [64] (reporting 20.4% efficiency at that time) (see [Table 4.1, 50]), and second, calibrated toward measured injection-dependent effective carrier lifetime curves of symmetrically passivated silicon wafers using heterojunction silicon thin-film layers as developed and characterized at SERIS (see [Tables 4.2 and 4.4, 50]) stated also in Appendix A.

Please note that especially the optical properties of the TCO have to be improved in order reach higher short-circuit current densities (i.e., compare J_{sc} values in the order of 37 mA · cm^{-2} as reported by Rahmouni/Taguchi [63], [64] and also if using the optical TCO and a-Si:H data published by EPFL [60], [61] to a J_{sc} of 39.5 mA · cm^{-2}, as recently reported by Panasonic [57]). Furthermore, the modeling assumes that the workfunction match of the TCO has been achieved, and thus, no TCO-induced band-bending reaching into the silicon bulk has to be considered. The optical properties depend strongly on the thickness and dielectric properties of the TCO and a-Si:H used. Here, a 70-nm-thick ITO is chosen as TCO, i.e., using optical TCO and a-Si:H data as published by Black and McIntosh [52]. Again note that currently the calibration toward measured lifetime samples

did not consider TCO. After a subsequent TCO optimization, a slight decrease in V_{oc} but an increase in J_{sc} can be expected.

In the conductive boundary modeling approach, the strongly nonideal effective recombination at the c-Si/a-Si interfaces requires to define an injection-dependent boundary recombination parameter J_0, fitted to lifetime measurements as explained above and parameterized as given in Appendix C. Also note that in the conductive boundary approach, the resistive losses due to current transport through the a-Si:H layers is accounted for by a (measured) contribution to the lumped series resistance.

Looking at the current loss analysis as sketched in Fig. 3, the front-contact shading is higher compared with other cells, as the grid has not been optimized toward a TCO (which is still to be optimized) yet. As expected for heterojunction solar cells, there is significant parasitic front-film absorption loss (TCO and a-Si:H), thereby reducing J_{sc}. The input parameters for the HJT cell are summarized in Table V.

E. PERL (UNSW): Record Efficiency Laboratory Silicon Solar Cell Fabricated at UNSW

The PERL cell, conceived and fabricated at the University of New South Wales (UNSW), held the 1-sun efficiency record of $25.0 \pm 0.5\%$ between 1998 and 2014 [65], [66]. It retains the 1-sun record for a diffused-junction silicon solar cell. The input parameters presented here are based on the data published in [67]–[70].

Notably, there is a discrepancy between the J_{sc} of the I–V measurement and the J_{sc} calculated from the QE and reflection measurements. The latter is 0.8 mA/cm^2 lower, although still within the uncertainty quoted for the I–V measurement. The discrepancy might be accounted for by differences in the optics between the location of the QE, reflection, and I–V measurements. For example, the tiler's pattern introduces a strong periodic dependence of the light trapping on cell width (amplitude of 0.4 mA/cm^2 and a period of $\sim$4 μm); thus, a variable cell width introduces spatially variable light trapping. Other spatial variations could arise from variability in scattering associated with roughened surfaces as well as variability in the planar regions between pyramids. In Table VI, the input parameters result in a J_{sc} that lies between that determined from I–V and QE measurements.

The refractive index of the original films was not published; here, we use data published in [44] and [64] to represent the original films, which yields a reflection curve consistent with the experimental curve for the stated film thicknesses.

Due to the large ratio of the perimeter-to-active cell area, the perimeter losses of the PERL cell are significant and constitute a loss in efficiency of about 0.2–0.3%, which is not taken into account in the results of Section IV. The input parameters for the PERL cell are summarized in Table VI.

F. IBC (ANU): High-Efficiency Laboratory Interdigitated-Back-Contact Solar Cell Fabricated at ANU

ANU's IBC cell with an efficiency of $24.4 \pm 0.7\%$ [77] is currently the most efficient IBC cell fabricated at a research institute. Although IBC cells with a higher efficiency have been

TABLE V
INPUT PARAMETER SET FOR THE HJT CELL

	cell design
cell size	156 mm $\times$ 156 mm pseudosquare thickness 150 μm
front	full-area i-a-Si:H/p-a-Si:H/TCO stackH-pattern screen-printed metallization
rear	full-area i-a-S:Hi/n-a-Si:H/TCO stackfull-area screen-printed metallization
	optics
front TCO	70-nm ITO with 2×10^{20} cm^{-3} free carrier density [61]
front a-Si:H	3.5-nm i-a-Si:H/6-nm p-a-Si:H, thicknesses from [58], optical properties from [60]
rear TCO	150-nm ITO with 6.5×10^{19} cm^{-3} free carrier density [61]
rear a-Si:H	3.5-nm i-a-Si:H/20-nm n-a-Si:H, thicknesses from [58], optical properties from [60]
front and rear morphology	random pyramids, 54.3° characteristic angle, 5-μm texture height
busbar shading fraction	2.86%
effective finger shading width	77 μm (= finger width times 70% effective shading [44])
	metal grid from [59]
front fingers	86 fingers with 1.7-mm-pitch, 110-μm–wide, and 13-μm-high Ag-based polymer paste with 7.15-$\mu\Omega \cdot$ cm effective resistivity (derived from measured sheet resistance and assuming rectangular cross sectional profile) contact resistivity 10 $\mu\Omega \cdot$ cm^2 (from [62]) lumped series resistance: 0.195 Ω cm^2
front busbars	3 busbars, 1500-μm-wide and 13-μm-high Ag-based polymer paste with 7.15-$\mu\Omega \cdot$ cm effective resistivity lumped series resistance: neglected
rear metal	full area Ag-based polymer paste contact resistivity 10 $\mu\Omega \cdot$ cm^2 (from [62]) lumped series resistance: negligible
	electrical properties
bulk	5-$\Omega \cdot$ cm n-type mid-gap SRH lifetimes $\tau_n = 1000\ \mu$s, $\tau_p = 10\,000\ \mu$s
front layers and interfaces	*lumped inputs* p+ boundary with sheet resistance 150 Ω (calculated from electron density and mobility given in [61]) parameterization of injection dependent recombination parameter J_0 as measured and derived at SERIS, see Appendix A3 Contribution to lumped series resistance of 0.16 $\Omega \cdot$ cm^2 *detailed inputs* summarized in [Tables 4.2 and 4.4, p. 85/88, 58]; see Appendix A1
rear layers and interfaces	*lumped inputs* n+ boundary, no value for sheet resistance required due to full area contact parameterization of injection dependent recombination parameter J_0 as measured and derived at SERIS; see Appendix A3 Negligible contribution to lumped series resistance *detailed inputs* summarized in [Tables 4.2 and 4.4, p. 85/88, 58]; see Appendix A1

published by Sunpower (25.0% [78]) and Panasonic (25.6% with heterojunction technology [56]), a comprehensive characterization and description of their properties is not publicly available, and consequently, input parameter sets of commercial IBC cells are not presented in this work.

The properties of ANU's IBC cell have been analyzed extensively and presented in [10], [77], [79], and [80]. The largest unknown in the input parameter set is the bulk lifetime of the device as it could not be measured nondestructively. The value presented in [77] was deduced by fitting the measured I–V curve

TABLE VI
INPUT PARAMETER SET FOR THE PERL CELL

	cell design
cell size	2 cm × 2 cm square
	thickness 425 μm
front	light full area n+ diffusion
	heavy n+ diffusion underneath fingers, 6.2-μm-wide
	line contact openings, 3-μm-wide
	photolithography-defined fingers, busbars outside of cell area
rear	undiffused and passivated
	square local n+ diffusion 30-μm-wide, 250-μm-pitch (266-μm x-pitch and 234-μm y-pitch for electrical unit cell modeling)
	aligned square contact openings 10-μm-wide
	full-area evaporated metallization
	optics based on [69]
front dielectrics	75-nm evaporated MgF$_2$ (outer ARC layer) n & k from [71] for single crystal MgF$_2$ (extraordinary rays)
	30-nm evaporated ZnS (inner ARC layer) n & k from [72] for evaporated hexagonal ZnS (extraordinary rays)
	25-nm thermal SiO$_2$ (passivation layer) n & k from [72] for thermal SiO$_2$
front morphology	regular inverted pyramids, 54.74° characteristic angle, 10 μm wide, tiler's pattern [73]
rear	planar rear with 200-nm SiO$_2$ coated with 3000-nm Al. n & k from [72] for thermal SiO$_2$ and pure Al.
effective finger shading width	12.8 μm (i.e., 64% of finger width [74])
	metal grid based on [68]
front fingers	25 fingers with 800-μm-pitch, 20-μm–wide, and 10-μm-high semicircular shape
	Ti/Pd/Al stack with 2.3-$\mu\Omega \cdot$cm effective resistivity
	contact resistivity 3-$\mu\Omega \cdot$cm^2
	lumped series resistance: 0.04 $\Omega \cdot$cm^2
rear metal	full-area pure Ag with 1.6 $\mu\Omega \cdot$cm resistivity, 10-μm-thick
	contact resistivity 1-$\mu\Omega \cdot$cm^2
	lumped series resistance: negligible
	electrical properties (based on [70], adjusted to material properties used in this work)
bulk	1-$\Omega \cdot$cm p-type
	mid-gap SRH lifetimes $\tau_n = \tau_p = 1200$ μs (fitted to measured V_{oc})
light front n+ diffusion	*lumped inputs*
	sheet resistance 195-Ω
	recombination parameter $J_0 = 6.1$ fA/cm^2
	depth 1-μm
	collection efficiency 0.997 (spectrum average)
	detailed inputs
	active doping profile
	Gaussian, 5×10^{18} cm^{-3} peak, 0-μm peak depth, 1 μm deep
	surface SRH
	$S_p = S_n = 298$ cm/s derived from [75] with a texture multiplier of 1.7
	volume SRH
	same as in bulk
heavy front n+ diffusion	*lumped inputs*
	sheet resistance 13 Ω
	recombination parameter J_0
	passivated: 97 fA/cm^2
	contacted: 118 fA/cm^2
	collection efficiency 0.79 (spectrum average)
	detailed inputs
	active doping profile
	Gaussian, 1×10^{20} cm^{-3} peak, 0-μm peak depth, 2 μm deep
	surface SRH
	$S_p = S_n = 2000$ cm/s (passivated)
	$S_p = S_n = 1 \times 10^7$ cm/s (contacted, thermal velocity)
	volume SRH
	same as in bulk

TABLE VI
(CONTINUED)

rear p+ diffusion	*lumped inputs*
	sheet resistance 13.6 Ω
	recombination parameter J_0
	passivated: 79 fA/cm^2
	contacted: 130 fA/cm^2
	depth 5 μm
	collection efficiency 0.85 (uniform generation)
	detailed inputs
	active doping profile
	Gaussian, 5×10^{19} cm^{-3} peak, 0-μm peak depth, 5 μm deep
	surface SRH
	passivated: $S_p = S_n = 2000$ cm/s
	contacted: $S_p = S_n = 1 \times 10^7$ cm/s (thermal velocity)
	volume SRH
	same as in bulk
passivated rear	*lumped inputs*
	S_{eff}: parameterization of data in [Fig. 6, 76]; see Appendix A3
	detailed inputs
	surface SRH and charge
	$S_p = 20$ cm/s, $S_n = 50$ cm/s, $Q = 7 \times 10^{10}$ cm^{-2}

to 3-D simulation *I–V* curve where the optical and surface recombination values are experimentally determined.

Some J_0 values presented in [77] have been slightly updated in this work to attain greater consistency, which notably required a reduction in the SRH lifetime in the bulk from 5 to 3 ms for a better overall agreement with measurements. There also exists some discrepancy between the measured BSF sheet resistance of 19 Ω/sq and simulation parameters in Table VII, to enable a good fit to the measured J_0 [77], which could otherwise not be achieved using any reasonable assumption for the doping profile. This discrepancy is likely a combination of experimental error in the sheet resistance and J_0 measurements. The change of sheet resistance is deemed insignificant to the internal resistance calculations due to the BSF being a 30-μm diameter local diffusion around the contacts; we, therefore, choose to fit the measured J_0 more accurately than the measured ρ_{sq}.

Similar as for the PERL cell, the perimeter losses of ANU's IBC cells are significant and have been characterized to contribute to 0.24% of the absolute efficiency loss, facilitated by accurate 3-D simulation based on the measured optical, electronic, and physical properties [77]. Since the simulation parameters do not include perimeter loss, this is a significant contributor to the observed discrepancy between measured and simulated efficiency, as presented in Table VIII. The input parameters for the IBC cell are summarized in Table VII.

IV. RESULTS

We now present the major outputs attained by simulating the solar cells using the input sets provided in the previous section. These outputs are presented as *I–V* parameters (see Table VIII), *I–V* curves (see Fig. 2), external quantum efficiency curves (see Fig. 3), current losses at maximum power (see Fig. 4), and resistive losses at maximum power (see Fig. 5).

TABLE VII
INPUT PARAMETER SET FOR THE IBC CELL

	cell design
cell size	2 cm × 2 cm square
	thickness 230 μm
front	undiffused and passivated
Rear	interdigitated diffusion pattern with 500-μm-pitch
	large-area p+ diffusion 330-μm-wide
	circular n+ diffusions 30-μm-wide, 70-μm pitch
	full-area passivation
	circular contact openings 7-μm-wide and 70-μm-pitch
	busbars outside of cell area

	optics
front dielectrics	*inner film*
	73-nm PECVD SiN$_x$ [80]
	outer film
	84-nm PECVD SiO$_x$ [80]
front morphology	random pyramids, 53° characteristic angle, 5-μm texture height
rear dielectrics	*inner film*
	30-nm thermal SiO$_2$ [72]
	outer film
	130-nm LPCVD Si$_3$N$_4$ [80]
rear morphology	Planar

	metal grid
p-fingers	40 fingers, 285-μm-wide and 4-μm-high
	pure Al with 2.8-$\mu\Omega \cdot$ cm resistivity
	contact resistivity 20-$\mu\Omega \cdot$ cm^2
	lumped series resistance: 0.016 $\Omega \cdot$ cm^2
n-fingers	40 fingers, 135-μm-wide and 4-μm-high
	pure Al with 2.8-$\mu\Omega \cdot$ cm resistivity
	contact resistivity 15-$\mu\Omega \cdot$ cm^2
	lumped series resistance: 0.035 $\Omega \cdot$ cm^2

	electrical properties
	taken from [70] adjusted to material properties used in this work
bulk	1.5-$\Omega \cdot$ cm n-type
	mid-gap SRH lifetimes $\tau_n = \tau_p = 3000$ μs (best match with measured *I–V* curve)
p+ diffusion	*lumped inputs*
	sheet resistance 166 Ω
	recombination parameter J_0
	passivated: 33.2 fA/cm^2
	contacted: 1234 fA/cm^2
	collection efficiency = 1
	detailed inputs
	active doping profile
	ERFC with 5.6 × 10^{19} cm^{-3} peak, 0-μm peak depth, 0.195-μm depth factor (PC1D definition), 0.6 μm deep
	surface SRH
	passivated: $S_p = S_n = 6850$ cm/s (fitted to measured J_0)
	contacted: $S_p = S_n = 1 \times 10^7$ cm/s (thermal velocity)
	volume SRH
	same as in bulk
n+ diffusion	*lumped inputs*
	sheet resistance 35 Ω
	recombination parameter J_0
	passivated: 176 fA/cm^2
	contacted: 202 fA/cm^2
	collection efficiency = 0.87 (uniform generation)
	detailed inputs
	active doping profile
	superposition of two ERFC's: 8 × 10^{19} cm^{-3}/4 × 10^{19} cm^{-3} peak, 0 μm/0 μm peak depth, 0.2 μm/0.5 μm depth factor (PC1D definition), 1.5 μm deep
	surface SRH
	passivated: $S_p = S_n = 1 \times 10^6$ cm/s (fitted to measured J_0)
	contacted: $S_p = S_n = 1 \times 10^7$ cm/s (thermal velocity)
	volume recombination
	same as in bulk

TABLE VII
(CONTINUED)

passivated front	*lumped inputs*
	recombination parameter $J_0 = 4.6$ fA/cm^2
	detailed inputs
	surface SRH and charge
	$Q = 5.6 \times 10^{11}$ cm^{-2}, $S_p = S_n = 2$ cm/s (derived from measured J_0 and charge, using case 3 in [81] and a texture multiplier of 1.7)
passivated rear	*lumped inputs*
	recombination parameter $J_0 = 19.5$ fA/cm^2
	detailed inputs
	surface SRH and charge
	$Q = 4 \times 10^{11}$ cm^{-2}, $S_p = S_n = 8$ cm/s (derived from measured J_0 and charge using case 3 in [81])

TABLE VIII
SUMMARY OF LIGHT *J–V* PARAMETERS SIMULATED BY QUOKKA USING THE INPUT PARAMETERS PRESENTED IN SECTION III

cell type	V_{oc} [mV]	J_{sc} [mA/cm^2]	FF [%]	η [%]
Conventional—simulated	626	35.2	79.8	17.6
PERC—simulated	655	39.8	79.4	20.7
n-Pasha—simulated	656	39.5	79.8	20.7
n-Pasha—measured (ECN in-house)	655	39.5	79.9	20.7
HJT—simulated	743	36.7	80.3	21.9
PERL—simulated	710	42.3	82.6	24.8
PERL—measured [66]	706	42.7	82.8	25.0
IBC—simulated	705	42.2	83.1	24.7
IBC—measured [77]	703	42.0	82.7	24.4

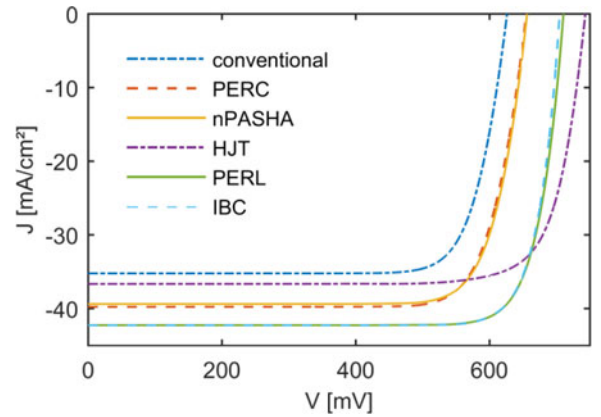Measured data are included for input sets that were derived from a specific experimental solar cell.

Fig. 2. Light *J–V* curves of the different cell types produced by Quokka simulations using the input parameters sets from this work.

The electrical component to the simulations followed the conductive boundary approach and was conducted with Quokka. The input files can be downloaded from [2]. Equivalent simulations using the detailed modeling approach (not shown) yield the same cell *I–V* parameters when the assumptions contained in the software are made identical and numerical errors are minimized.

We emphasize that it is not the purpose of the following comparisons to rate different cell technologies. Some of the simulations represent industrial designs while others represent
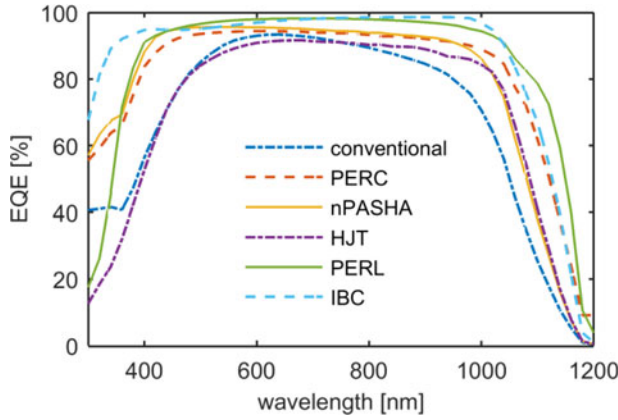
Fig. 3. External quantum efficiencies of the different cell types produced by Quokka simulations using the input parameters sets from this work; note that busbar shading is included.
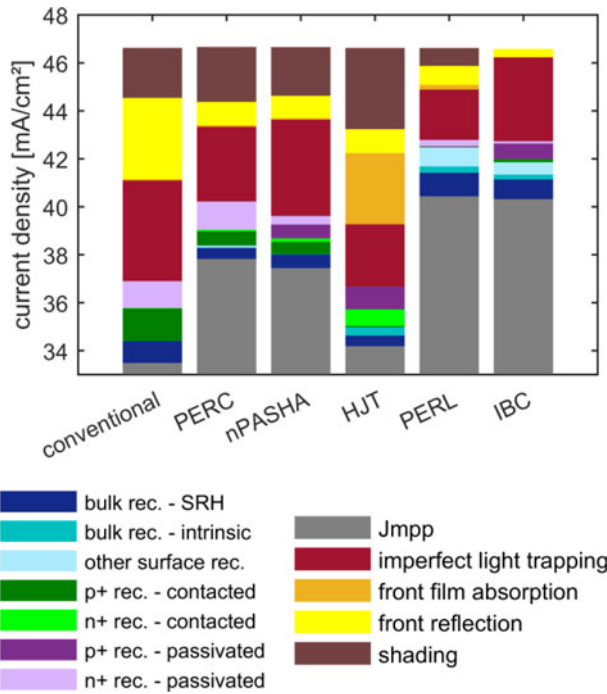

Fig. 5. Resistive power loss breakdown at maximum power point.

Fig. 4. Current loss breakdown at maximum power point, categorized into output current J_{mpp}, recombination losses (*left legend*), and optical losses (*right legend*).

V. CONCLUSION

The many intricacies inherent to solar cell modeling make it difficult—but all the more valuable—to provide a reference point on which PV researchers can base their cell simulations.

In this work, we have contributed toward that goal by providing input parameter sets to simulate six specific c-Si solar cells, as well as the methodologies, assumptions, and physical models that accompany those inputs. As far as possible, we ensure the input parameters to be justified, typical, and to produce typical and measured cell characteristics.

Once more we emphasize that the parameter sets cannot be used to represent all cells of a given architecture. Some sets are specific to small-area laboratory-based cells, others to large-area industrial cells. In addition, due to variability in material quality and imperfect manufacturing repeatability, the parameter sets represent just one cell within a wide distribution of cells made by identical processing sequences. Moreover, changes to the input sets and methodologies cannot be made indiscriminately. Many input values depend on the choice of physical model, e.g., the values selected for the surface recombination velocities depend on the Auger and bandgap narrowing model. Simulation experts are encouraged to critically examine the justifications and substitute their own values where appropriate.

The input sets are accessible from an online library [2]. We hope that through examination, discussion, and experimentation, they will be continually reviewed, revised, and extended to provide an up-to-date reference for the PV community to simulate c-Si solar cells with ever more accuracy.

APPENDIX A
INPUT PARAMETERS FOR DETAILED MODELING OF THE HJT (PROJECTED) CELL

For better accessibility, excerpts of [Tables 4.2 and 4.4, 58] are given in Tables IX and X, which list the electrical input

small-area laboratory solar cells (PERL, IBC). Thus, the results do not enable a meaningful comparison between the potential of the different cell architectures.

The results indicate that the simulated *I–V* parameters agree closely with those of the n-Pasha, PERL, and IBC cells that were used to represent each respective cell type. By a comparison of the losses, the relative difference between the cell types is clear. For example, the higher J_{sc} of the PERL cells is due mainly to its low grid reflection and its superior light trapping. In addition, as another example, the advantage of the very high V_{oc} attained by the heterojunction cell is partially offset by a high parasitic absorption in the front films.
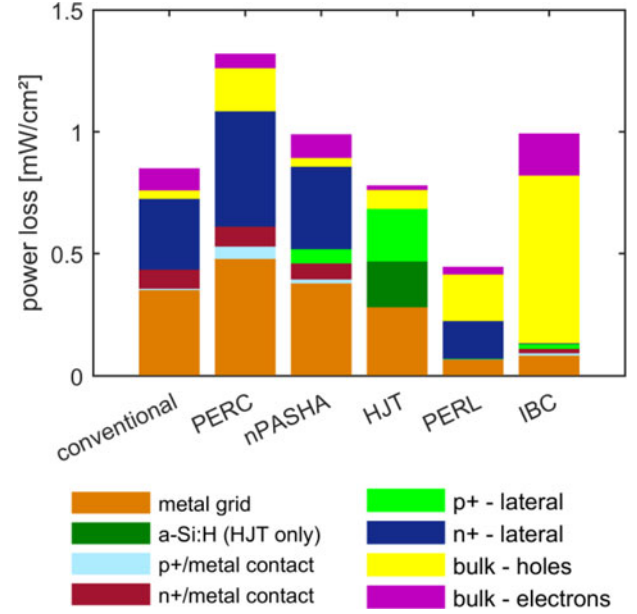
TABLE IX
EXCERPT OF [TABLE 4.2, 58]

Parameters	a-Si:H(i)	a-Si:H(n)	a-Si:H(p)
Layer thickness (μm)	0.005	0.020	0.020
Electron affinity (eV)	4.0	4.0	4.0
Mobility gap (eV)	1.75	1.80	1.75
ΔE_V with respect to c-Si (eV)	−0.41	−0.46	−0.41
Donor (acceptor) doping (cm^{-3})	0	1.45×10^{19}	(1.41×10^{19})
Effective DOS in CB (cm^{-3})	2×10^{20}	2×10^{20}	2×10^{20}
Effective DOS in VB (cm^{-3})	2×10^{20}	2×10^{20}	2×10^{20}
Urbach energy (VB tail) (eV)	0.045	0.05	0.05
Urbach energy (CB tail) (eV)	0.03	0.03	0.03
Urbach tail pre-factor(cm$^{-3} \cdot$ eV^{-1})	4×10^{21}	4×10^{21}	4×10^{21}
Electron/hole mobility (cm$^2 \cdot$ V$^{-1} \cdot$ s^{-1})	25/5	20/4	25/5
Gaussian defect density (cm^{-3})	9×10^{16}	2.75×10^{19}	2.63×10^{19}
Gaussian donor peak position from VB (eV)	0.83	0.50	1.00
Gaussian acceptor peak position from VB (eV)	1.03	0.70	1.20
Neutral σ (for Urbach tail and Gaussian defects) (cm^2)	10^{-15}	6.5×10^{-16}	6.5×10^{-16}
Charged σ (for Urbach tail and Gaussian defects) (cm^2)	10^{-14}	6.5×10^{-15}	6.5×10^{-15}
Activation energy (eV)	0.83	0.20	0.30
Correlation energy (eV)	0.20	0.20	0.20

TABLE X
[TABLE 4.4, 58]

Lifetime structure	[i/N/i] c-Si(n)/a-Si:H(i)	[p/i/N/i/p] c-Si(n)/a-Si:H(i, p)	[n/i/N/i/n] c-Si(n)/a-Si:H(i, n)
Interface	a-Si/c-Si interface	a-Si/c-Si interface	a-Si/c-Si interface
D_{it} (cm$^{-2} \cdot$ eV^{-1})	4.6×10^{12}	5×10^{10}	5×10^{10}
Charged σ (cm^2)	10^{-18}	10^{-18}	10^{-18}
Neutral σ (cm^2)	10^{-19}	10^{-19}	10^{-19}

parameters for the detailed modeling of the a-Si:H films and interfaces as used for the HJT cell.

APPENDIX B
DOPING PROFILES

Figs. 6 and 7 show the emitter and BSF profiles of the conventional and PERC cell type assumed in this work.
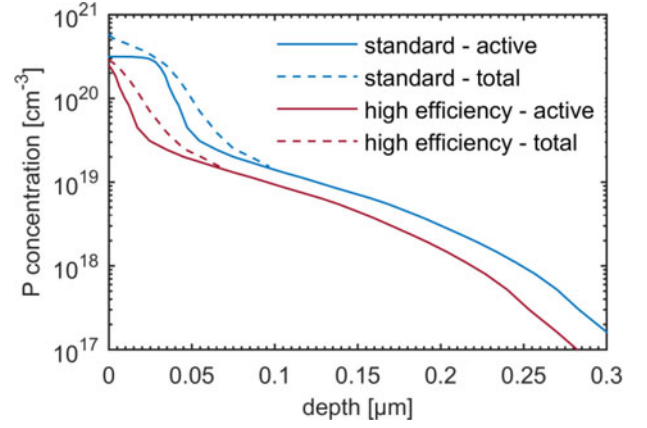

Fig. 6. Phosphorous concentration profiles of the front n$^+$ regions (emitter) of the "standard" (taken from [38]) and "high efficiency" emitter as used for the conventional and PERC cell type, respectively; note that the "high efficiency" profile is derived by thinning the "standard" profile by 30 nm, representing an etch-back process.
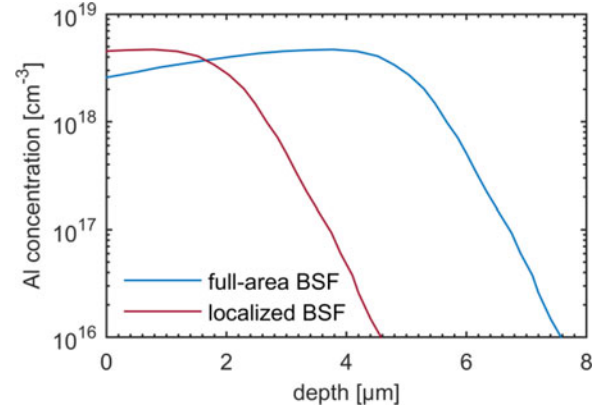

Fig. 7. Al concentration profiles of the rear p$^+$ regions (BSF) of the full-area BSF (conventional cell) and local BSF region (PERC cell); note that the local BSF profile is derived by thinning the full-area one by 3 μm.

APPENDIX C
PARAMETERIZATIONS

A. Front and Rear J_0 of HJT (Projected) Cell

The injection-dependent J_0 of the a-Si:H boundaries were extracted by numerical simulations of measured effective lifetime, which also match the detailed modeling, and numerically fitted by a second-order Fourier expression. Here, $\Delta p[\text{cm}^{-3}]$ denotes the excess carrier density at the boundary

$$
\begin{aligned}
J_{o,\text{front}} \left[\frac{A}{\text{cm}^2} \right] = &\left(\frac{8.27}{8.52} \right)^2 \\
&\cdot 10^{\wedge}((1.367 + 0.7028 \cos(\log(\Delta p)) \\
&+ 0.2459 \sin(\log(\Delta p)) \\
&- 0.04068 \cos(2\log(\Delta p)) \\
&- 0.2271 \sin(2\log(\Delta p)))
\end{aligned}
$$

$$J_{o,\text{rear}}\left[\frac{\text{A}}{\text{cm}^2}\right] = \left(\frac{8.27}{8.52}\right)^2$$

$$\cdot 10 \wedge (1.029 + 0.293\cos(1.304\log(\Delta p))$$

$$- 0.5323\sin(1.304\log(\Delta p))$$

$$+ 0.01279\cos(2.608\log(\Delta p))$$

$$+ 0.1621\sin(2.608\log(\Delta p))).$$

B. Rear S_{eff} of the PERL (UNSW) Cell

The best fit to the data in [Fig. 6, 76] was achieved by the following double exponential function, where $\Delta n[\text{cm}^{-3}]$ denotes the excess carrier density at the boundary:

$$S_{\text{eff}}\left[\frac{\text{cm}}{\text{s}}\right] = 10 \wedge \left(3.262 \times 10^{14}\right.$$

$$\exp\left(-\left(\frac{\log(\Delta n) + 395.3}{71.14}\right)^2\right)$$

$$\left.+ 1.35\exp\left(-\left(\frac{\log(\Delta n) - 10.88}{2.229}\right)^2\right)\right).$$

REFERENCES

[1] A. Fell *et al.*, "Input parameters for the simulation of silicon solar cells in 2014," presented at the 6th World Conf. Photovoltaic Energy Convers., Kyoto, Japan, 2014.

[2] (2015). *PV Lighthouse Solar Cell Library*. [Online]. Available: http://pvlighthouse.com.au/resources/solar%20cell%20library/solar%20cell%20library.aspx

[3] Synopsys, *Sentaurus: Sentaurus Device User Guide, Release H-2013.03*, 2013.

[4] (2015). *PV Lighthouse*. [Online]. Available: http://pvlighthouse.com.au

[5] S. C. Baker-Finch and K. R. McIntosh, "One-dimensional photogeneration profiles in silicon solar cells with pyramidal texture," *Progr. Photovoltaics: Res. Appl.*, vol. 20, pp. 51–61, 2012.

[6] A. Fell and K. R. McIntosh, "Deriving the generation profile for silicon solar cells from lumped optical parameters," presented at the 42rd IEEE Photovoltaic Spec. Conf., New Orleans, LA, USA, 2015.

[7] P. A. Basore, "Numerical modeling of textured silicon solar cells using PC-1D," *IEEE Trans. Electron Devices*, vol. 37, no. 2, pp. 337–343, Feb. 1990.

[8] A. Fell, "A free and fast three-dimensional/two-dimensional solar cell simulator featuring conductive boundary and quasi-neutrality approximations," *IEEE Trans. Electron Devices*, vol. 60, no. 2, pp. 733–738, Feb. 2013.

[9] A. Goetzberger, J. Knobloch, B. Voss, and R. Waddington, *Crystalline Silicon Solar Cells*. Chichester, U.K.: Wiley, 1998.

[10] A. Fell, K. C. Fong, K. R. McIntosh, E. Franklin, and A. W. Blakers, "3-D simulation of interdigitated-back-contact silicon solar cells with quokka including perimeter losses," *IEEE J. Photovoltaics*, vol. 4, no. 4, pp. 1040–1045, Jul. 2014.

[11] R. Brendel, "Modeling solar cells with the dopant-diffused layers treated as conductive boundaries," *Progr. Photovoltaics: Res. Appl.*, vol. 20, pp. 31–43, 2012.

[12] P. A. Basore and K. Cabanas-Holmen, "PC2D: A circular-reference spreadsheet solar cell device simulator," *IEEE J. Photovoltaics*, vol. 1, no. 1, pp. 72–77, Jul. 2011.

[13] A. Cuevas and R. A. Sinton, "Detailed modelling of silicon solar cells," in *Proc. 23rd Eur. Photovoltaic Sol. Energy Conf.*, Valencia, Spain, 2008, pp. 315–319.

[14] A. Cuevas, "Physical model of back line-contact front-junction solar cells," *J. Appl. Phys.*, vol. 113, p. 164502, 2013.

[15] (2014). *Atlas Device Simulator*, Silvaco Int. Softw., Santa Clara, CA, USA.

[16] K. R. McIntosh and P. P. Altermatt, "A freeware 1D emitter model for silicon solar cells," in *Proc. 35th IEEE Photovoltaic Spec. Conf.*, 2010, pp. 002188–002193.

[17] M. Padilla *et al.*, "Surface recombination parameters of interdigitated-back-contact silicon solar cells obtained by modeling luminescence images," *Sol. Energy Mater. Sol. Cells*, vol. 120, Part A, pp. 363–375, 2014.

[18] K. Rapolu, P. Singh, and S. Shea, "Two dimensional numerical modeling of a silicon solar cell with selective emitter configuration," in *Proc. 35th IEEE Photovoltaic Spec. Conf.*, 2010, pp. 002227–002232.

[19] D. A. Clugston and P. A. Basore, "PC1D version 5: 32-bit solar cell modeling on personal computers," in *Proc. 26th IEEE Photovoltaic Spec. Conf.*, 1997, pp. 207–210.

[20] H. Haug, A. Kimmerle, J. Greulich, A. Wolf, and E. Stensrud Marstein, "Implementation of Fermi–Dirac statistics and advanced models in PC1D for precise simulations of silicon solar cells," *Sol. Energy Mater. Sol. Cells*, vol. 131, pp. 30–36, Dec. 2014.

[21] P. P. Altermatt, "Models for numerical device simulations of crystalline silicon solar cells—A review," *J. Comput. Electron.*, vol. 10, pp. 314–330, Sep. 2011.

[22] D. E. Kane and R. M. Swanson, "Measurement of the emitter saturation current by a contactless photoconductivity decay method," in *Proc. 18th IEEE Photovoltaic Spec. Conf.*, 1985, pp. 578–583.

[23] K. Misiakos and D. Tsamakis, "Accurate measurements of the silicon intrinsic carrier density from 78 to 340 K," *J. Appl. Phys.*, vol. 74, pp. 3293–3297, 1993.

[24] P. P. Altermatt, A. Schenk, F. Geelhaar, and G. Heiser, "Reassessment of the intrinsic carrier density in crystalline silicon in view of band-gap narrowing," *J. Appl. Phys.*, vol. 93, pp. 1598–1604, 2003.

[25] A. Schenk, "Finite-temperature full random-phase approximation model of band gap narrowing for silicon device simulation," *J. Appl. Phys.*, vol. 84, pp. 3684–3695, 1998.

[26] A. Richter, S. W. Glunz, F. Werner, J. Schmidt, and A. Cuevas, "Improved quantitative description of Auger recombination in crystalline silicon," *Phys. Rev. B*, vol. 86, p. 165202, 2012.

[27] T. Trupke *et al.*, "Temperature dependence of the radiative recombination coefficient of intrinsic crystalline silicon," *J. Appl. Phys.*, vol. 94, pp. 4930–4937, 2003.

[28] D. B. M. Klaassen, "A unified mobility model for device simulation—I. Model equations and concentration dependence," *Solid-State Electron.*, vol. 35, pp. 953–959, 1992.

[29] C. Gueymard, *SMARTS2: A Simple Model of the Atmospheric Radiative Transfer of Sunshine: Algorithms and Performance Assessment*, Cocoa, FL, USA: Florida Solar Energy Cent., 1995.

[30] M. A. Green, "Self-consistent optical parameters of intrinsic silicon at 300K including temperature coefficients," *Sol. Energy Mater. Sol. Cells*, vol. 92, pp. 1305–1310, 2008.

[31] S. P. Group, *International Technology Roadmap for Photovoltaic*, Mar. 2014.

[32] M. Abbott, G. Scardera, K. R. McIntosh, and A. Meisel, "Simulation of emitter doping profiles formed by industrial POCl3 processes," in *Proc. IEEE 39th Photovoltaic Spec. Conf.*, 2013, pp. 1383–1388.

[33] Y. Li, Z. Li, Y. Zhao, and A. Lennon, "Modelling of light trapping in acidic-textured multicrystalline silicon wafers," *Int. J. Photoenergy*, vol. 2012, p. 369101, 2012.

[34] S. C. Baker-Finch, K. R. McIntosh, and M. L. Terry, "Isotextured silicon solar cell analysis and modeling 1: Optics," *IEEE J. Photovoltaics*, vol. 2, no. 4, pp. 457–464, Oct. 2012.

[35] J. Greulich *et al.*, "Optical simulation and analysis of iso-textured silicon solar cells including light trapping," presented at the 5th Int. Conf. Crystalline Silicon Photovoltaics, Constance, Germany, 2015.

[36] B. T. Phong, "Illumination for computer generated pictures," *Commun. ACM*, vol. 18, pp. 311–317, 1975.

[37] M. Abbott *et al.*, "Silicon ink selective emitter solar cells on multicrystalline silicon wafers," presented at the 25th Photovoltaic Sol. Energy Conf. Exhib. Conf., Valencia, Spain, 2010.

[38] A. Dastgheib-Shirazi, M. Steyer, G. Micard, H. Wagner, P. P. Altermatt, and G. Hahn, "Relationships between diffusion parameters and phosphorus precipitation during the POCl$_3$ diffusion process," *Energy Procedia*, vol. 38, pp. 254–262, 2013.

[39] B. Min, H. Wagner, A. Dastgheib Shirazi, A. Kimmerle, H. Kurz, and P. P. Altermatt, "Heavily doped Si: P emitters of crystalline Si solar cells: recombination due to phosphorus precipitation," *Phys. Status Solidi (RRL)—Rapid Res. Lett.*, vol. 8, pp. 680–684, 2014.

[40] R. Bock, P. P. Altermatt, J. Schmidt, and R. Brendel, "Formation of aluminum–oxygen complexes in highly aluminum-doped silicon," *Semicond. Sci. Technol.*, vol. 25, p. 105007, 2010.

[41] M. Rüdiger, M. Rauer, C. Schmiga, and M. Hermle, "Effect of incomplete ionization for the description of highly aluminum-doped silicon," *J. Appl. phys.*, vol. 110, p. 024508, 2011.

[42] P. Rosenits, T. Roth, and S. W. Glunz, "Erratum on "Determining the defect parameters of the deep aluminum-related defect center in silicon [Appl. Phys. Lett. 91, 122109 (2007)]," *Appl. Phys. Lett.*, vol. 99, p. 239904, 2011.

[43] S. Duttagupta, F. Ma, B. Hoex, T. Mueller, and A. G. Aberle, "Optimised antireflection coatings using silicon nitride on textured silicon surfaces based on measurements and multidimensional modelling," *Energy Procedia*, vol. 15, pp. 78–83, 2012.

[44] R. Woehl, M. Hörteis, and S. Glunz, "Determination of the effective optical width of screen printed and aerosol printed and plated fingers," in *Proc. 23rd Eur. Photovoltaic Sol. Energy Conf. Exhib.*, 2008, pp. 1377–1382.

[45] M. Rüdiger, C. Schmiga, M. Rauer, M. Hermle, and S. W. Glunz, "Efficiency potential of n-type silicon solar cells with aluminum-doped rear p+ emitter," *IEEE Trans. Electron Devices*, vol. 59, no. 5, pp. 1295–1303, May 2012.

[46] M. Rüdiger, C. Schmiga, M. Rauer, M. Hermle, and S. W. Glunz, "Optimisation of industrial n-type silicon solar cells with aluminium-alloyed rear emitter by means of 2D numerical simulation," in *Proc. 25th Eur. Photovoltaic Sol. Energy Conf. Exhib.*, Valencia, Spain, 2010, pp. 2280–2286.

[47] J. Schmidt *et al.*, "Impurity-related limitations of next-generation industrial silicon solar cells," in *Proc. IEEE 38th Photovoltaic Spec. Conf.*, 2012, pp. 1–5.

[48] J. Greulich, N. Wöhrle, M. Glatthaar, and S. Rein, "Optical modeling of the rear surface roughness of passivated silicon solar cells," *Energy Procedia*, vol. 27, pp. 234–239, 2012.

[49] N. Wohrle, J. Greulich, C. Schwab, M. Glatthaar, and S. Rein, "A predictive optical simulation model for the rear-surface roughness of passivated silicon solar cells," *IEEE J. Photovoltaics*, vol. 3, no. 1, pp. 175–182, Jan. 2013.

[50] S. C. Baker-Finch, K. R. McIntosh, M. L. Terry, and Y. Wan, "Isotextured silicon solar cell analysis and modeling 2: Recombination and device modeling," *IEEE J. Photovoltaics*, vol. 2, no. 4, pp. 465–472, Oct. 2012.

[51] P. Saint-Cast, D. Kania, M. Hofmann, J. Benick, J. Rentsch, and R. Preu, "Very low surface recombination velocity on p-type c-Si by high-rate plasma-deposited aluminum oxide," *Appl. Phys. Lett.*, vol. 95, pp. 151502-1–151502-3, 2009.

[52] L. E. Black and K. R. McIntosh, "Modeling recombination at the Si–AlO interface," *IEEE J. Photovoltaics*, vol. 3, no. 3, pp. 936–943, Jul. 2013.

[53] I. Romijn, A. Gutjahr, D. Saynova, J. Anker, E. Kossen, and K. Tool, "Cost effective n-Pasha solar cells with efficiency above 20%," *Photovoltaics Int.*, vol. 20, pp. 33–40, 2013.

[54] A. Burgers *et al.*, "19.5% efficient n-type Si solar cells made in production," in *Proc. 26th Eur. Photovoltaic Sol. Energy Conf.*, 2011, pp. 1144–1147.

[55] G. J. M. Janssen, A. Gutjahr, A. R. Burgers, D. S. Saynova, I. Cesar, and I. G. Romijn, "Power loss analysis of n-PASHA cells validated by 2D simulations," in *Proc. 28th Eur. Photovoltaic Sol. Energy Conf. Exhib.*, Paris, France, 2013, pp. 1548–1553.

[56] K. Masuko *et al.*, "Achievement of more than 25% conversion efficiency with crystalline silicon heterojunction solar cell," *IEEE J. Photovoltaics*, vol. 4, no. 6, pp. 1433–1435, Nov. 2014.

[57] M. A. Green, K. Emery, Y. Hishikawa, W. Warta, and E. D. Dunlop, "Solar cell efficiency tables (version 42)," *Progr. Photovoltaics: Res. Appl.*, vol. 21, pp. 827–837, 2013.

[58] L. Zhepeng, "Design, fabrication and characterisation of thin-film materials for heterojunction silicon wafer solar cells," Ph.D. dissertation, Dept. Elect. Comput. Eng., Univ. Singapore, Singapore, 2014.

[59] A. Khanna, Z. P. Ling, V. Shanmugam, M. B. Boreland, I. Hayashi, D. Kirk *et al.*, "Screen printed metallisation for silicon heterojunction solar cells," in *Proc. 28th Eur. Photovoltaic Sol. Energy Conf. Exhib.*, Paris, France, 2013, pp. 1336–1339.

[60] Z. C. Holman, A. Descoeudres, L. Barraud, F. Z. Fernandez, J. P. Seif, S. De Wolf *et al.*, "Current losses at the front of silicon heterojunction solar cells," *IEEE J. Photovoltaics*, vol. 2, no. 1, pp. 7–15, Jan. 2012.

[61] Z. C. Holman, M. Filipič, A. Descoeudres, S. De Wolf, F. Smole, M. Topič *et al.*, "Infrared light management in high-efficiency silicon heterojunction and rear-passivated solar cells," *J. Appl. Phys.*, vol. 113, p. 013107, 2013.

[62] J. Geissbuhler, S. De Wolf, A. Faes, N. Badel, Q. Jeangros, A. Tomasi *et al.*, "Silicon heterojunction solar cells with copper-plated grid electrodes: Status and comparison with silver thick-film techniques," *IEEE J. Photovoltaics*, vol. 4, no. 4, pp. 1055–1062, Jul. 2014.

[63] M. Rahmouni, A. Datta, P. Chatterjee, J. Damon-Lacoste, C. Ballif, and P. R. I Cabarrocas, "Carrier transport and sensitivity issues in heterojunction with intrinsic thin layer solar cells on N-type crystalline silicon: A computer simulation study," *J. Appl. Phys.*, vol. 107, p. 054521, 2010.

[64] M. Taguchi, E. Maruyama, and M. Tanaka, "Temperature dependence of amorphous/crystalline silicon heterojunction solar cells," *Jpn. J. Appl. Phys.*, vol. 47, p. 814, 2008.

[65] J. Zhao, A. Wang, M. A. Green, and F. Ferrazza, "19.8% efficient "honeycomb" textured multicrystalline and 24.4% monocrystalline silicon solar cells," *Appl. Phys. Lett.*, vol. 73, pp. 1991–1993, 1998.

[66] J. Zhao, A. Wang, and M. A. Green, "24·5% efficiency silicon PERT cells on MCz substrates and 24·7% efficiency PERL cells on FZ substrates," *Progr. Photovoltaics: Res. Appl.*, vol. 7, pp. 471–474, 1999.

[67] A. G. Aberle, P. P. Altermatt, G. Heiser, S. J. Robinson, A. Wang, J. Zhao, *et al.*, "Limiting loss mechanisms in 23% efficient silicon solar cells," *J. Appl. Phys.*, vol. 77, pp. 3491–3504, 1995.

[68] P. P. Altermatt, G. Heiser, A. G. Aberle, A. Wang, J. Zhao, S. J. Robinson, *et al.*, "Spatially resolved analysis and minimization of resistive losses in high-efficiency Si solar cells," *Progr. Photovoltaics: Res. Appl.*, vol. 4, pp. 399–414, 1996.

[69] J. Zhao and M. A. Green, "Optimized antireflection coatings for high-efficiency silicon solar cells," *IEEE Trans. Electron Devices*, vol. 38, no. 8, pp. 1925–1934, Aug. 1991.

[70] P. P. Altermatt, G. Heiser, and M. A. Green, "Numerical quantification and minimization of perimeter losses in high-efficiency silicon solar cells," *Progr. Photovoltaics: Res. Appl.*, vol. 4, pp. 355–367, 1996.

[71] M. J. Dodge, "Refractive properties of magnesium fluoride," *Appl. Opt.*, vol. 23, pp. 1980–1985, 1984.

[72] E. D. Palik, Ed., *Handbook of Optical Constants of Solids (Academic Press Handbook Series)*, vol. 1. New York, NY, USA: Academic, 1985.

[73] P. Campbell and M. A. Green, "Light trapping properties of pyramidally textured surfaces," *J. Appl. Phys.*, vol. 62, pp. 243–249, 1987.

[74] A. Blakers, "Shading losses of solar-cell metal grids," *J. Appl. Phys.*, vol. 71, pp. 5237–5241, 1992.

[75] P. P. Altermatt, J. O. Schumacher, A. Cuevas, M. J. Kerr, S. W. Glunz, R. R. King, *et al.*, "Numerical modeling of highly doped Si:P emitters based on Fermi–Dirac statistics and self-consistent material parameters," *J. Appl. Phys.*, vol. 92, pp. 3187–3197, 2002.

[76] S. J. Robinson, S. R. Wenham, P. P. Altermatt, A. G. Aberle, G. Heiser, and M. A. Green, "Recombination rate saturation mechanisms at oxidized surfaces of high-efficiency silicon solar cells," *J. Appl. Phys.*, vol. 78, pp. 4740–4754, 1995.

[77] E. Franklin, *et al.*, "Design, fabrication and characterisation of a 24.4% efficient interdigitated back contact solar cell," *Progr. Photovoltaics: Res. Appl.*, 2014. doi: 10.1002/pip.2556

[78] D. D. Smith, P. Cousins, S. Westerberg, R. D. Jesus-Tabajonda, G. Aniero, and Y. Shen, "Toward the practical limits of silicon solar cells," *IEEE J. Photovoltaics*, vol. 4, no. 6, pp. 1465–1469, Nov. 2014.

[79] K. C. Fong, K. Teng, K. R. McIntosh, A. W. Blakers, E. Franklin, N. Zin, *et al.*, "N+ diffusion and contact optimisation of IBC solar cells," presented at the 28th Eur. PV Sol. Energy Conf., Paris, France, 2013.

[80] K. R. McIntosh *et al.*, "Quantifying the optical losses in back-contact solar cells," in *Proc. IEEE 40th Photovoltaic Spec. Conf.*, 2014, pp. 0115–0123.

[81] K. R. McIntosh and L. E. Black, "On effective surface recombination parameters," *J. Appl. Phys.*, vol. 116, p. 014503, 2014.

Authors' photographs and biographies not available at the time of publication.